Broadband Impedance Shaping Control Scheme of MMC-Based STATCOM for Improving the Stability of the Wind Farm

Yang Zhang, *Member, IEEE*, Yuqing Wang, Donghui Zhang, Xin Chen, *Member, IEEE*, and Chunying Gong, *Member, IEEE*

***Abstract*—Sub and super-synchronous resonance problems caused by the increasing penetration of wind energy in the grid usually can be solved by reshaping the impedance of wind farms. Considering the feasibility and economics, the static synchronous compensator (STATCOM), which is already part of the wind farm in certain regions, becomes a preferred option for impedance shaping to improve the system stability. However, due to the difference between the application object and the application scenario, the control schemes for impedance shaping that widely used in the two-level voltage source converter are difficult to apply directly to the MMC-based STATCOM to solve the resonance problems in the practical wind farm. Therefore, in this article, a broadband impedance shaping control scheme for MMC-based STATCOM is proposed to generate an active parallel impedance, thus reshaping the impedance characteristics of the wind farm over the sub and super-synchronous frequencies for enhancing the system stability. Then, a passivity-based design method for this impedance is developed to ensure that the proposed control can provide sufficient damping at the desired frequency. With this broadband impedance shaping control scheme, the STATCOM can effectively suppress resonance in the wind farm under various operation conditions, which is confirmed by the hardware-in-the-loop experimental results.**

***Index Terms*—Broadband impedance shaping control scheme, hardware-in-the-loop (HIL) platform, stability, STATCOM, wind farm.**

I. Introduction

SUB and super-synchronous resonance problem caused by the increasing penetration of wind energy in the grid challenges regional electricity security. In 2009, an approximately 20-Hz resonance between the type-III wind turbine generators (WTGs) and the grid with series compensation systems was reported by ERCOT in the USA [1]. Since 2011, many similar events with the resonant frequency of 3 to 10 Hz have been observed in the wind farm in Guyuan, China [2]. In recent years, subsynchronous resonances at 20 to 40 Hz and accompanying super-synchronous resonances at 60 to 80 Hz involving type-IV WTGs and static synchronous compensator (STATCOM) connected to a weak grid were also recorded in Hami, China [3], [4].

These sub and super-synchronous resonance problems can be analyzed by applying the impedance-based stability criterion to the developed output impedance model of the WTGs and the grid [5], [6]. In the wind farms connected to the ac grid, the controls of the WTGs are usually employed to shape their impedances in order to suppress the system resonance [7]–[9]. Nevertheless, due to the various control designs and complex operating conditions of the WTGs, such a method may be ineffective or even unfeasible in practice. In this case, an additional active damper in the wind farm is an effective option for damping the wind farm resonance [10], [11], but the consequential additional costs for the purchase and maintenance have also prevented the widespread application of such specialized stabilizers. Hence, the STATCOM, which is already part of the wind farm in certain regions to provide reactive power support and voltage regulation, is considered as a preference used to enhance the system stability. The ability of STATCOM that can suppress the subsynchronous resonance of type-III WTGs connected to a series-compensated line has been demonstrated by adding the auxiliary damping control in the STATCOM [12], [13]. However, this conventional auxiliary damping control requires accurate remote measurements, and is also not suitable for solving the high-frequency resonance problem in wind farms.

In recent years, the impacts of the STATCOM on the stability of the grid or wind farms were investigated based on the impedance-based analysis method to suppress the sub and super-synchronous resonances using the damping provided by the STATCOM impedance [14]–[17]. Yet, the exploration of how to shape the STATCOM impedance to improve the system damping is relatively preliminary. Similar to the methods used in other voltage source converters (VSCs), the STATCOM impedance characteristics at certain frequencies can be effectively improved by regulating the parameters in corresponding control, e.g., phase-locked loop (PLL) and module capacitor voltage control, thereby damping system resonance [15], [17]–[19]. Since the

Manuscript received November 15, 2020; revised January 14, 2021 and March 10, 2021; accepted March 14, 2021. Date of publication March 17, 2021; date of current version June 1, 2021. This work was supported in part by the Science and Technology Project of State Grid Corporation of China under Project SGTYHT/19-JS-215, in part by the National Natural Science Foundation of China under Grant 51877105, and in part by the Jiangsu Postgraduate Research and Practical Innovation Project (KYLX16_0360). *(Corresponding author: Xin Chen.)*

The authors are with the Jiangsu Key Laboratory of New Energy Generation and Power Conversion, Nanjing University of Aeronautics and Astronautics, Nanjing 210016, China (e-mail: youngzhang@nuaa.edu.cn; wyq_nuaa@163.com; ceozdhceo@nuaa.edu.cn; chen.xin@nuaa.edu.cn; zjnjgcy@nuaa.edu.cn).

Color versions of one or more figures in this article are available at https://doi.org/10.1109/TPEL.2021.3066631.

Digital Object Identifier 10.1109/TPEL.2021.3066631

effects of these controls on the impedance characteristics, especially at the sub and super-synchronous frequencies, are coupled to each other [4], it is difficult to obtain the optimal STATCOM impedance by designing the parameters of one or in turn several controllers. To address this problem, the heuristic intelligence algorithm is used in the impedance optimization design to synchronously solve the parameters of multiple controllers for the optimal system stability margin [19]. Nevertheless, limited by the control structure and the performance requirements in the practical STATCOM design, there is little room left for the STATCOM impedance optimization to obtain the optimal system stability-robustness.

Compared to the aforementioned methods, a better approach for impedance shaping is to incorporate additional active controls that create the desired damping effects, which has been widely used in the two-level grid-connected VSC to damp the resonance caused by the LCL-type filters [20]–[22] and to enhance their adaptability to the weak grid [23]–[25]. However, these active control methods are difficult to apply directly to the STATCOM to solve the sub and super-synchronous resonance problems in the practical wind farm. The main reasons are as follows.

1) Most control methods were only capable of narrow-band shaping of the converter impedance for certain frequencies (usually focused on the medium- and high-frequencies), which makes it difficult to achieve the impedance control with strong robustness against the variations of the operating condition covering the sub and super-synchronous frequencies.
2) Those control methods proposed for two-level VSCs did not consider the impacts of the multiharmonic characteristics and frequency coupling effect of modular multilevel converters (MMCs), which have been widely used in medium- and high-voltage STATCOM applications, on the effectiveness of impedance shaping controls.
3) The core idea of the existing control methods is to compensate the phase of the converter impedance at the intersection frequency of the impedance of the interactive system, but due to the power level limitation, when using the STATCOM to damp the system resonance, in addition to the phase compensation, the amplitude of the STATCOM impedance must be regulated accordingly, which greatly increases the difficulty of the design of STATCOM impedance shaping control.

Thus, to overcome the above limitations and achieve the objective of damping the sub and super-synchronous resonance in the practical wind farm and improving the system stability-robustness, a broadband impedance shaping control scheme for MMC-based STATCOM is proposed in this article. This proposed control takes into account the impacts of the multiharmonic characteristics of MMC and frequency coupling effect and generates an active impedance in parallel with the STATCOM output impedance, to achieve the impedance control of wind farm over a wide frequency range, especially covering the sub and super-synchronous frequencies. Additionally, to simplify the design of the parallel impedance created by the proposed control, a passivity-based design method for this impedance is also developed to ensure that the proposed control can provide sufficient damping over the entire sub and synchronous frequency range. The rest of the article is organized as follows. Section II reviews the sequence impedance matrix models of the MMC-based STATCOM. Section III presents a quantitative stability analysis for practical wind farms. Section IV proposes a broadband impedance shaping control scheme of MMC-based STATCOM. Section V presents the design of the broadband impedance shaping controller by developing a passivity-based design method. The effectiveness of the proposed impedance shaping control scheme is verified by the experimental results based on hardware-in-the-loop (HIL) platform in Section VI. Finally, Section VI concludes the article.

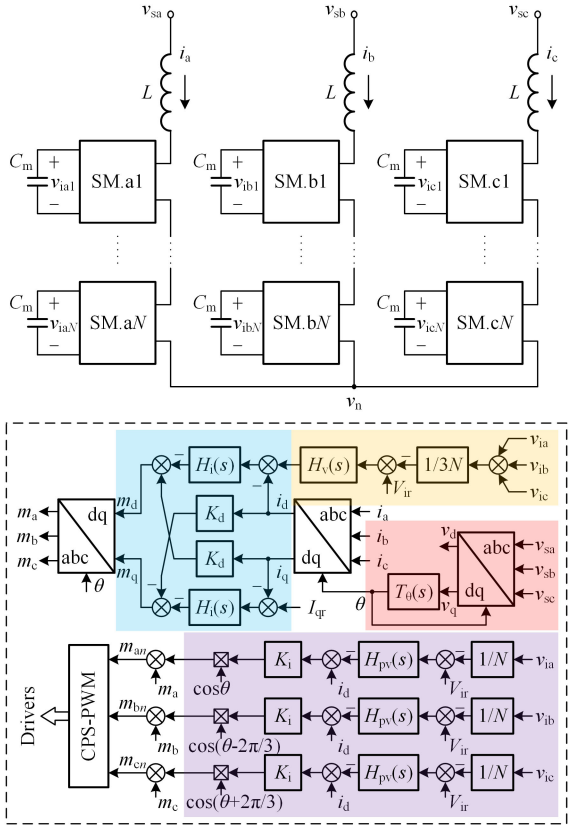

Fig. 1. Power stage circuit and control diagram of the STATCOM in a single-star MMC (SM – submodule).

II. Modeling of STATCOM in Single-Star MMC

Fig. 1 shows the power stage circuit and control diagrams of the STATCOM in a single-star MMC (also called cascaded H-bridge topology) [26]. As shown in Fig. 1, v_{sx} (x = a, b, c) represents the three-phase output terminal voltages, i_x (x = a, b, c) denotes the three-phase arm (phase) currents, and v_{ixn} (x = a, b, c; n = 1, …, N) is the three-phase submodule capacitor voltages with L being the arm inductor and C_m being the submodule capacitor. Since the cell (individual) voltage balancing control does not affect the converter dynamics [27], only the average voltage control, phase (clustered) voltage balancing control, *dq*-frame phase current control, and PLL are presented,

where V_{ir} and I_{qr} represent the reference of average module capacitor voltage and reactive current, respectively, $v_{\mathrm{i}x}$ (x = a, b, c) indicates the sum of module capacitor voltages in each phase, and θ is the angle generated from the PLL.

The small-signal matrix model of the single-star MMC-based STATCOM in Fig. 1 has been developed according to the double-harmonic linearization in [17], of which the power stage model can be expressed as

$$\hat{\mathbf{i}} = \mathbf{Y}_{\mathrm{l}}[\hat{\mathbf{v}}_{\mathrm{p}} - (\mathbf{M}\hat{\mathbf{v}}_{\mathrm{i}} + \mathbf{V}_{\mathrm{i}}\hat{\mathbf{m}})] \tag{1}$$

$$\hat{\mathbf{v}}_{\mathrm{i}} = \mathbf{Z}_{\mathrm{c}}(\mathbf{M}\hat{\mathbf{i}} + \mathbf{I}\hat{\mathbf{m}}) \tag{2}$$

where $\hat{\mathbf{m}}$, $\hat{\mathbf{i}}$, $\hat{\mathbf{v}}_{\mathrm{i}}$, and $\hat{\mathbf{v}}_{\mathrm{p}}$ are the vectors for small-signal responses of insertion index, phase current, equivalent module capacitor voltage, and terminal voltage, respectively [17]. $\mathbf{Y}_{\mathrm{l}}$ and $\mathbf{Z}_{\mathrm{c}}$ are the small-signal admittance of the arm inductor and the small-signal impedance of the equivalent module, respectively, and are capacitor, denoted as

$$\mathbf{Y}_{\mathrm{l}} = \frac{1}{L}\mathrm{diag}\left(\frac{1}{s-2j\omega_1}, 0, \frac{1}{s}, \frac{1}{s+j\omega_1}, 0\right)$$

$$\mathbf{Z}_{\mathrm{c}} = \frac{N}{C_{\mathrm{m}}}\mathrm{diag}\left(\frac{1}{s+jn\omega_1}|_{n=-2,-1,0,1,2}\right)$$

where ω_1 is the fundamental angular frequency.

M and **I** representing the steady-state harmonic matrix of the insertion index and phase current, respectively, are both 5 $\times$ 5 tri-diagonal matrices with the main diagonal elements as zero, the elements in the diagonal above the main diagonal as $M_1\mathrm{e}^{-j\sigma_1}$ ($I_1\mathrm{e}^{-j\alpha_1}$), and the elements in the diagonal below the main diagonal as $M_1\mathrm{e}^{j\sigma_1}$ ($I_1\mathrm{e}^{j\alpha_1}$) ($M_1$ (I_1) and σ_1 (α_1) are the amplitude and phase of the Fourier coefficient of the insertion index (phase current) at ω_1). $\mathbf{V}_{\mathrm{i}}$ representing the steady-state harmonic matrix of the sum of the submodule capacitor voltages in one phase, is a 5 $\times$ 5 matrix with the main diagonal elements as $V_{\mathrm{i}0}$ (the Fourier coefficient of equivalent module capacitor voltage at dc), the $(n, n+2)|_{n=1,2,3}$-th elements as $V_{\mathrm{i}2}\mathrm{e}^{-j\beta_2}$, the $(n+2, n)|_{n=1,2,3}$-th elements as $V_{\mathrm{i}2}\mathrm{e}^{j\beta_2}$, and the rest elements as zero ($V_{\mathrm{i}2}$ and β_2 are, respectively the amplitude and phase of the Fourier coefficient of the module capacitor voltage at $2\omega_1$).

Accordingly, the control model can be expressed as

$$\hat{\mathbf{m}} = \mathbf{E}\hat{\mathbf{v}}_{\mathrm{i}} + \mathbf{Q}\hat{\mathbf{i}} + \mathbf{P}\hat{\mathbf{v}}_{\mathrm{p}} \tag{3}$$

where **E** representing the control gain matrix related to the module capacitor voltage, is a 5 $\times$ 5 zero matrix except for the $(n+1, n+2)|_{n=0,2}$-th, denoted as

$$\frac{\mathrm{e}^{-j\varphi_1}}{2N}\left[K_{\mathrm{i}}H_{\mathrm{pv}}(s+j(n-1)\omega_1) + \frac{(2-n)}{2}H_{\mathrm{v}}(s-j\omega_1)H_{\mathrm{i}}(s-j\omega_1)\right]$$

and $(n+3, n+2)|_{n=0,2}$-th elements, denoted as

$$\frac{\mathrm{e}^{j\varphi_1}}{2N}\left[K_{\mathrm{i}}H_{\mathrm{pv}}(s+j(n-1)\omega_1) + \frac{(2-n)}{2}H_{\mathrm{v}}(s-j\omega_1)H_{\mathrm{i}}(s-j\omega_1)\right].$$

Q representing the control gain matrix related to the phase current, is a 5 $\times$ 5 matrix, of which all elements are zero except for the $(1, n+1)|_{n=0,2}$-th, denoted as

$$\frac{(2-n)}{2}\left[H_{\mathrm{i}}(s-j\omega_1) + jK_{\mathrm{d}}\right] + \mathrm{e}^{-jn\varphi_1}\frac{K_{\mathrm{i}}}{2}$$

and $(3, n+1)|_{n=0,2}$-th elements, denoted as

$$\frac{n}{2}\left[H_{\mathrm{i}}(s-j\omega_1) + jK_{\mathrm{d}}\right] + \mathrm{e}^{j(2-n)\varphi_1}\frac{K_{\mathrm{i}}}{2}.$$

P representing the control gain matrix related to the terminal voltage, is a 5 $\times$ 5 zero matrix except for the (1, 3)-th and (3, 3)-th elements, denoted, respectively, as

$$\begin{aligned}
&\mathrm{e}^{-j\varphi_1}G_\theta(s-j\omega_1)\cdot\\
&\Big[I_1\mathrm{e}^{-j\alpha_1}[H_{\mathrm{i}}(s-j\omega_1)+jK_{\mathrm{d}}] - M_1\mathrm{e}^{-j\sigma_1}\\
&+\frac{I_1(\mathrm{e}^{-j\alpha_1}-\mathrm{e}^{j(\alpha_1-2\varphi_1)})}{2}K_{\mathrm{i}}\Big]\\
&-\mathrm{e}^{-j\varphi_1}G_\theta(s-j\omega_1)\cdot\\
&\Big[I_1\mathrm{e}^{j\alpha_1}[H_{\mathrm{i}}(s-j\omega_1)-jK_{\mathrm{d}}] - M_1\mathrm{e}^{j\sigma_1}\\
&+\frac{I_1(\mathrm{e}^{j\alpha_1}-\mathrm{e}^{-j(\alpha_1-2\varphi_1)})}{2}K_{\mathrm{i}}\Big]
\end{aligned}$$

where $G_\theta(s) = T_\theta(s)/(1+V_{\mathrm{s}1}T_\theta(s))$, $T_\theta(s) = H_\theta(s)/s$, and V_1 and φ_1 are the amplitude and phase of the fundamental output terminal voltage, respectively.

Based on (1)–(3), the sequence equivalent model of the STATCOM in a single-star MMC in matrix form can be derived as presented in Fig. 2(a). Then, Fig. 2(a) can be transformed into Fig. 2(b) by the equivalent transformation of the control block diagram, where the transfer matrices are defined as

$$\mathbf{G}_{\mathrm{x}1} = (\mathbf{U} - \mathbf{E}\mathbf{Z}_{\mathrm{c}}\mathbf{I})^{-1}(\mathbf{Q} + \mathbf{E}\mathbf{Z}_{\mathrm{c}}\mathbf{M}) \tag{4}$$

$$\mathbf{G}_{\mathrm{x}2} = \mathbf{M}\mathbf{Z}_{\mathrm{c}}\mathbf{I} + \mathbf{V}_{\mathrm{i}} \tag{5}$$

$$\mathbf{G}_{\mathrm{x}3} = (\mathbf{U} + \mathbf{Y}_{\mathrm{l}}\mathbf{M}\mathbf{Z}_{\mathrm{c}}\mathbf{M})^{-1}\mathbf{Y}_{\mathrm{l}} \tag{6}$$

$$\mathbf{G}_{\mathrm{y}1} = (\mathbf{U} - \mathbf{E}\mathbf{Z}_{\mathrm{c}}\mathbf{I})^{-1}\mathbf{P}. \tag{7}$$

Furthermore, moving the feedback node of $\hat{\mathbf{i}}$ and the forward node of $\hat{\mathbf{v}}_{\mathrm{p}}$ to the input of $\mathbf{G}_{\mathrm{x}3}$, obtains Fig. 2(c). Therefore, the admittance coefficient matrix of the STATCOM in a single-star MMC can be defined by

$$\hat{\mathbf{i}} = \mathbf{Y}_{\mathrm{ST}}\hat{\mathbf{v}}_{\mathrm{p}} \tag{8}$$

in which

$$\mathbf{Y}_{\mathrm{ST}} = (\mathbf{U} + \mathbf{G}_{\mathrm{x}3}\mathbf{G}_{\mathrm{x}2}\mathbf{G}_{\mathrm{x}1})^{-1}\mathbf{G}_{\mathrm{x}3}(\mathbf{U} - \mathbf{G}_{\mathrm{x}2}\mathbf{G}_{\mathrm{y}1}). \tag{9}$$

It is noted that the elements in the third column of (9) indicate that the transfer functions from the voltage perturbation at ω_{p} to the phase current responses at $\omega_{\mathrm{p}} \pm n\omega_1$ (n = 0, 1, 2). Since most of these elements are zero, or have a negligible impact on the system stability, only the (1, 3)-th and the (3, 3)-th elements are

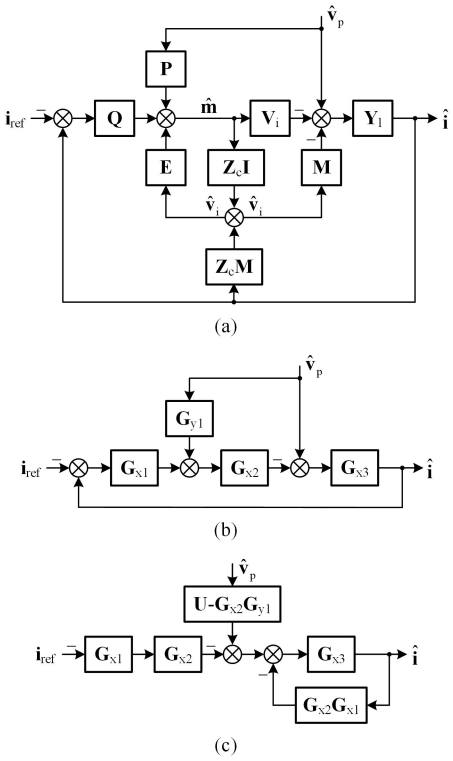

Fig. 2. Sequence equivalent control block diagram of the single-star MMC-based STATCOM in matrix form (a), and its (b) transformation I and (c) transformation II.

considered and defined as the transfer function of coupling term $Y_c(s)$ from the perturbation voltage to the phase current response at $\omega_p - 2\omega_1$ and the transfer function of original admittance $Y_p(s)$ from the perturbation voltage to the phase current response at ω_p, respectively [19].

III. Stability Analysis of Wind Farm

A typical wind farm involving the single-star MMC-based STATCOM in Western China is presented in this article to account for the impedance-based system stability analysis. As shown in Fig. 3, three or four 4.5-MW WTGs—each WTG is aggregated from three 1.5-MW type-IV WTGs [28] with shunt filter capacitors and 620-V/35-kV step-up transformers are connected in a string by the power cables. Three strings are collected at the 35-kV bus to feed power into the transmission network, which is simplified as a transmission line connected to a voltage source through the 35-kV/110-kV and 110-kV/220-kV transformers. One 10-MVA STATCOM in a single-star MMC is integrated in the wind farm, and it is directly connected to the 35-kV bus. The circuit and control diagram of the aggregated type-IV WTG is presented in Fig. 4, and the detailed parameters of the STATCOM, aggregated type-IV WTG and the wind farm system are listed in Tables I, II, and III, respectively.

Considering the variable operation conditions of the wind farm, three cases for the stability analysis of the wind farm are presented in Table IV. In Case 1, the 1st string is not connected to the 35-kV bus, thus the number of WTGs operating

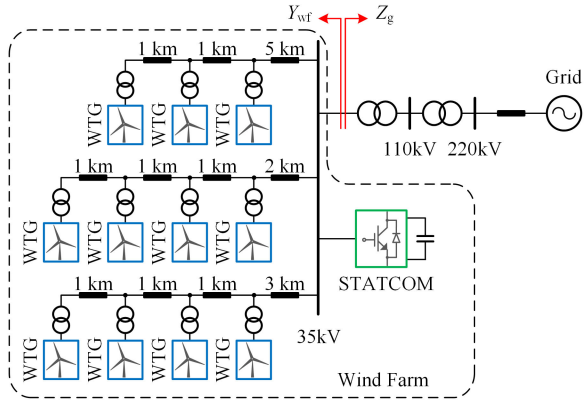

Fig. 3. Configuration of a typical wind farm involving the single-star MMC-based STATCOM in Western China.

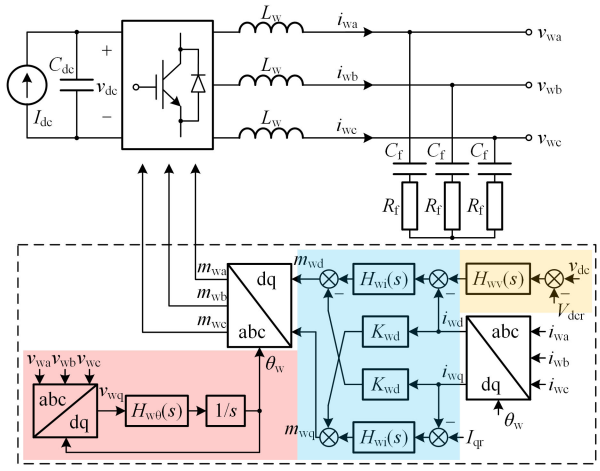

Fig. 4. Circuit and control diagram of the aggregated type-IV WTG.

TABLE I
Parameters of 10-MVA STATCOM

Parameters	Values
Number of Modules per Arm N	36
Arm Inductance L	78 mH
Submodule Capacitance C_m	1.5 mF
Cell Capacitor Voltage V_{in}	1000 V
Grid L-L Voltage (RMS)	35 kV @ 50 Hz
Phase Current Controller	$H_i(s) = 3.69\times10^{-4} + 0.50 / s$
PLL Controller	$H_\theta(s) = 8.68\times10^{-3} + 0.60 / s$
Average Voltage Controller	$H_v(s) = 2.24\times10^{-1} + 19.0 / s$
Phase Voltage Balancing Controller	$H_{pv}(s) = 5.92\times10^{-2} + 1.08 / s$ $K_i = 1.14\times10^{-4}$

TABLE II
Parameters of 4.5-MW Aggregated Type-IV WTG

Parameters	Values
Filter Inductance L_w	60 μH
Filter Capacitance C_f	1.95 mF
Damping Resistance R_f	0.01 Ω
DC-Link Capacitance C_{dc}	90 mF
DC-Link Voltage V_{dc}	1200 V
Grid L-L Voltage (RMS)	620 V @ 50 Hz
Phase Current Controller	$H_{wi}(s) = 2.59\times10^{-5} + 4.73\times10^{-2} / s$
PLL Controller	$H_{w\theta}(s) = 3.71\times10^{-2} + 19.70 / s$
DC-Link Voltage Controller	$H_{wv}(s) = 4.38 + 4.69\times10^{2} / s$

TABLE III
ELECTRICAL PARAMETERS OF STUDIED WIND FARM SYSTEM

Parameters		Values
620-V / 35-kV Transformer	Turns Ratio	31/1750
	Short Circuit Impedance	$45.06\times10^{-3}s + 3.54$
35-kV / 110-kV Transformer	Turns Ratio	7/22
	Short Circuit Impedance	$67.79\times10^{-3}s + 2.66$
110-kV / 220-kV Transformer	Turns Ratio	1/2
	Short Circuit Impedance	$0.29s + 5.64$
35-kV Power Cables	Resistance	0.13 Ω / km
	Inductance	1.27 mH / km

TABLE IV
OPERATION CONDITION OF STUDIED WIND FARM

		Case 1	Case 2	Case 3
Output Power of WTGs in the 1st String / p.u.			0.263	0.632
Output Power of WTGs in the 2nd String / p.u.		0.592	0.539	0.592
Output Power of WTGs in the 3rd String / p.u.		0.552	0.503	0.552
Output Power of STATCOM / p.u.		0.220	0.442	0.220
220kV Overhead Lines	Equivalent Resistance / Ω	3.02	3.02	4.24
	Equivalent Inductance / H	0.96	0.96	1.35
SCR at the PCC of Wind Farm		2.0	2.0	1.6

in this condition is reduced to 8. In Case 2, all three strings are connected to the 35-kV bus, and the output power of WTGs in the second and third string is decreased slightly with the wind speed. Accordingly, the STATCOM will produce more reactive power to maintain the PCC voltage. In Case 3, all three strings are connected to the 35-kV bus with the boosted output power of WTGs in 1st string, and the short circuit ratio (SCR) at the PCC of the wind farm is significantly reduced.

Since the zeros of the determinant of the frequency-domain nodal admittance matrix of the studied system are equivalent to its eigenvalues [29], the stability of this wind farm is easily known from the impedance network matrix model of the entire wind farm system [30]. In Case 1, there are two right-half-plane (RHP) zeros, which are $4.8163 + 60.2727j$ and $4.8163 + 568.0458j$. This indicates the system is unstable and the predicted resonance frequencies are 9.6 and 90.4 Hz, respectively. In Case 2, the RHP zeros are $3.8884 + 97.7387j$ and $3.8884 + 530.5798j$, which means there is a risk of potential resonance with 15.6 Hz- and 84.4 Hz-resonance frequencies. In Case 3, the RHP zeros are $5.3960 \times 10^{-3} + 197.2166j$ and $5.3960 \times 10^{-3} + 431.1019j$, showing instability. The corresponding predicted resonance frequencies are 31.4 and 68.6 Hz.

To further obtain the quantitative system stability margin, the method for the quantitative stability analysis of wind farms presented in [19] is adopted. Through impedance aggregation, the wind farm system can be illustrated in the two-coupled equivalent circuits for the responses at ω_p and $\omega_p - 2\omega_1$, respectively, as shown in Fig. 5(a) and (b), where $Z_g(s)$ represents the grid-side impedance, $Y_{wfp}(s)$ represents the original admittance of the wind farm, and $Y_{wfc}(s)$ represents the coupling term of the wind farm. Then, the two coupling equivalent circuits can

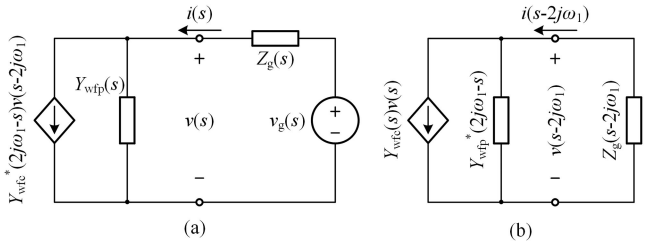

Fig. 5. Equivalent circuit of the wind farm system for (a) responses at ω_p and (b) responses at $\omega_p - 2\omega_1$.

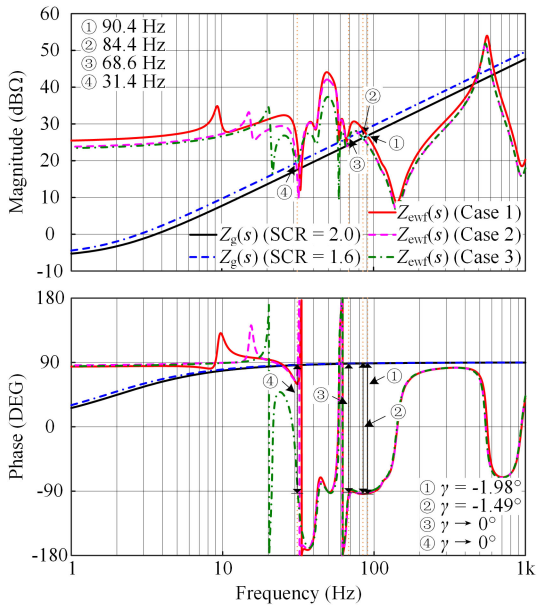

Fig. 6. Frequency responses of $Z_g(s)$ and $Z_{ewf}(s)$ for studied cases.

be further reduced to an equivalent circuit for the single-input-single-output (SISO) system. Finally, the stability of the injected currents of the wind farm can be determined by the equivalent impedance ratio $Z_g(s)Y_{ewf}(s)$, where the equivalent admittance of wind farm $Y_{ewf}(s)$ is denoted as

$$Y_{ewf}(s) = Y_{wfp}(s) - \frac{Y_{wfc}(s)Y_{wfc}{}^*(2j\omega_1 - s)}{Y_{wfp}{}^*(2j\omega_1 - s) + 1/Z_g(s - 2j\omega_1)} \tag{10}$$

in which the superscript "$*$" indicates a conjugation. Accordingly, the stability margin γ can be evaluated quantitatively by

$$\gamma = 180^\circ - [\arg(Z_g(j\omega_i)) - \arg(Z_{ewf}(j\omega_i))]$$

where ω_i is the intersection frequency of $Z_g(s)$ and $Z_{ewf}(s)$ ($Z_{ewf}(s) = Y_{ewf}{}^{-1}(s)$).

Fig. 6 shows the frequency responses of $Z_g(s)$ and $Z_{ewf}(s)$ for the cases in Table IV. In Case 1, the stability margin at the intersection frequency (90.4 Hz) of $Z_g(s)$ and $Z_{ewf}(s)$ is –1.98°, and an RHP pole in $Y_{ewf}(s)$ is $5.0747 + 60.3877j$. In Case 2, there is an intersection of the two impedance responses with –1.49°-stability margin at 84.4 Hz, in addition to an RHP pole in $Y_{ewf}(s)$, which is $4.0784 + 98.1446j$. In Case 3, the intersections with an almost 0°-stability margin at 31.4 and 68.6 Hz will affect

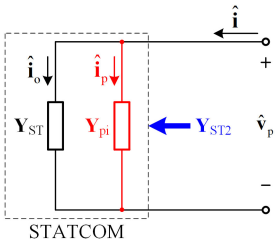

Fig. 7. Matrix equivalent circuit of the single-star MMC-based STATCOM with an additional parallel impedance.

the system stability. Obviously, the above analysis shows that there is a risk of resonance or even instability of the system in these three cases, and such stability conclusions and predicted resonance frequencies are consistent with the results of the system eigenvalue analysis.

It can be seen from Fig. 6 that the insufficient or even negative stability margin, which is caused by the negative damping effects (the phase responses of impedances are less than –90°) of the PLL and dc-side voltage control of those converters in the wind farm on the equivalent impedance of the wind farm $Z_{\rm ewf}(s)$ below 100 Hz [19], will lead to sub and super-synchronous resonances in wind farms. Thus, to improve the stability of the wind farm, it is necessary to introduce an additional damping in the wind farm to mitigate the effects of the negative damping characteristics on $Z_{\rm ewf}(s)$ at these frequencies.

IV. Broadband Impedance Shaping Control Scheme

Adding a parallel passive impedance at the point of common coupling (PCC) of the wind farm may be an approach to enhance the damping of the equivalent impedance of the entire wind farm and then improve the system stability. However, the shortcomings of this approach are obvious, e.g., additional cost and power loss, and poor flexibility. To avoid these, such a passive impedance can be implemented by an active control for impedance shaping in the converter [31]. Since the MMC-based STATCOM which has been directly installed at the PCC of the wind farm in Fig. 3, is a preferred objective to achieve this control, a broadband impedance shaping control scheme for MMC is proposed in this section.

A. Development of Shaping Control With Parallel Impedance

According to (8), the equivalent circuit in the matrix form of the MMC-based STATCOM with an additional parallel impedance is illustrated in Fig. 7, and its corresponding admittance coefficient matrix can be expressed as

$$\mathbf{Y}_{\rm ST2} = \mathbf{Y}_{\rm ST} + \mathbf{Y}_{\rm pi}$$

where $\mathbf{Y}_{\rm pi}$ represents the admittance coefficient matrix for $Y_{\rm pi}(s)$, denoted as

$$\mathbf{Y}_{\rm pi} = \mathrm{diag}(Y_{\rm pi}(s + jn\omega_1)|_{n=-2,-1,0,1,2}).$$

Based on Fig. 2(c), the equivalent transformation II of control block diagram for the MMC-based STATCOM with the parallel impedance in Fig. 7 can be presented in Fig. 8(a). Then, the equivalent transformation I of the control block diagram presented in Fig. 8(b) can be obtained by moving the node of $\hat{\mathbf{i}}_{\rm p}$ from the output of $\mathbf{G}_{\rm x3}$ to the input of $\mathbf{G}_{\rm x2}$, which becomes a feedforward node of $\hat{\mathbf{v}}_{\rm p}$, and then restoring the feedback node of $\hat{\mathbf{i}}$ to the input of $\mathbf{G}_{\rm x1}$. In Fig. 8(b), the transfer matrix $\mathbf{G}_{\rm y2}$ is expressed as

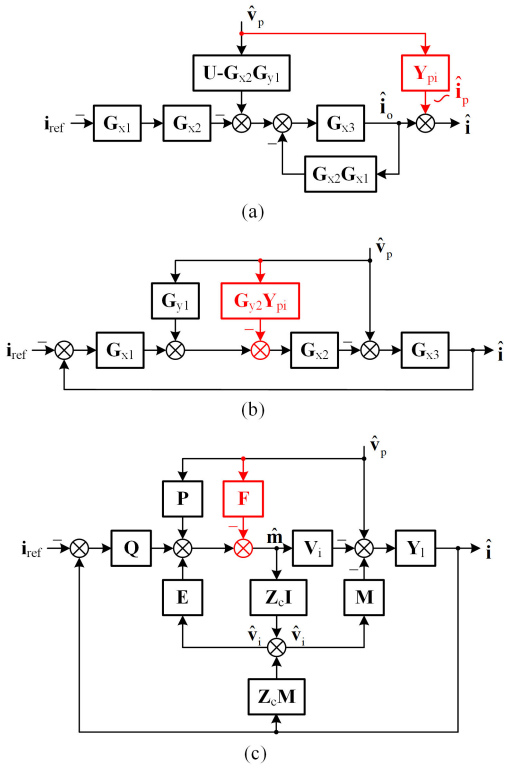

Fig. 8. Sequence equivalent control block diagram of the single-star MMC-based STATCOM with the parallel impedance: (a) transformation II, (b) transformation I, and (c) matrix form with a voltage feedforward control.

$$\mathbf{G}_{\rm y2} = {\mathbf{G}_{\rm x2}}^{-1}{\mathbf{G}_{\rm x3}}^{-1} + \mathbf{G}_{\rm x1}. \tag{11}$$

Referring to Fig. 2(a), the control block diagram of Fig. 8(b) can be further transformed to be Fig. 8(c) to obtain the small-signal model of a voltage feedforward control, which is

$$\hat{\mathbf{m}} = -\mathbf{F}\hat{\mathbf{v}}_{\rm p} \tag{12}$$

in which $\mathbf{F}$ is the control gain matrix, expressed as

$$\mathbf{F} = (\mathbf{U} - \mathbf{E}\mathbf{Z}_{\rm c}\mathbf{I})\mathbf{G}_{\rm y2}\mathbf{Y}_{\rm pi}. \tag{13}$$

Substituting (4)–(6) and (11) into (13) and using $\mathbf{Z}_{\rm l}$ to replace ${\mathbf{Y}_{\rm l}}^{-1}$ to facilitate the mathematical tractability, result in that

$$\mathbf{F} = \mathbf{T}\mathbf{Y}_{\rm pi} \tag{14}$$

where

$$\mathbf{T} = (\mathbf{U} - \mathbf{E}\mathbf{Z}_{\rm c}\mathbf{I})(\mathbf{M}\mathbf{Z}_{\rm c}\mathbf{I} + \mathbf{V}_{\rm i})^{-1}(\mathbf{Z}_{\rm l} + \mathbf{M}\mathbf{Z}_{\rm c}\mathbf{M}) + \mathbf{Q} + \mathbf{E}\mathbf{Z}_{\rm c}\mathbf{M}$$

$$\mathbf{Z}_{\rm l} = \mathrm{diag}((s + jn\omega_1)L|_{n=-2,-1,0,1,2}).$$

Therefore, introducing a voltage feedforward control, namely impedance shaping control, whose control gain matrix satisfies (14) in the STATCOM is equivalent to creating an admittance $Y_{\mathrm{pi}}(s)$ in parallel with the STATCOM output admittance. Theoretically, based on the (1, 3)-th and (3, 3)-th elements of $\mathbf{F}$ in (14) that affect the frequency responses of the coupling term $Y_{\mathrm{c}}(s)$ and original admittance $Y_{\mathrm{p}}(s)$ of the STATCOM, the transfer function, and implementation of the impedance shaping control can be easily developed in inverse. However, for the MMC applications, such a derivation is difficult to implement directly due to the fact that the expressions of the elements in the transfer matrix $\mathbf{T}$ are usually too complex. Therefore, to obtain the transfer function of the impedance shaping control that can be implemented, it is necessary to simplify the transfer matrix $\mathbf{T}$.

B. Simplification of Transfer Matrix for Shaping Control

Although the expressions of the elements in the transfer matrix $\mathbf{T}$ are complex, not all terms in the expressions have a significant effect on the frequency characteristics of the elements in the transfer matrix over a certain frequency range. Therefore, the transfer matrix $\mathbf{T}$ can be simplified by ignoring some matrices or terms in the expressions that have less effect in the frequency range of interest, thus ensuring that the frequency responses of the elements in the transfer matrix remain similar before and after the simplification.

Based on (1)–(3), the impedance coefficient matrix of the STATCOM without the PLL can be obtained by removing the matrix $\mathbf{P}$ in (3), as

$$\mathbf{Z} = (\mathbf{Z}_{\mathrm{l}} + \mathbf{M}\mathbf{Z}_{\mathrm{c}}\mathbf{M}) + (\mathbf{M}\mathbf{Z}_{\mathrm{c}}\mathbf{I} + \mathbf{V}_{\mathrm{i}}) \cdot (\mathbf{U} - \mathbf{E}\mathbf{Z}_{\mathrm{c}}\mathbf{I})^{-1}(\mathbf{Q} + \mathbf{E}\mathbf{Z}_{\mathrm{c}}\mathbf{M}).$$

Thus the transfer matrix $\mathbf{T}$ in (14) can be rewritten as

$$\mathbf{T} = (\mathbf{U} - \mathbf{E}\mathbf{Z}_{\mathrm{c}}\mathbf{I})(\mathbf{M}\mathbf{Z}_{\mathrm{c}}\mathbf{I} + \mathbf{V}_{\mathrm{i}})^{-1}\mathbf{Z}.$$

Since the elements in $(\mathbf{U} - \mathbf{E}\mathbf{Z}_{\mathrm{c}}\mathbf{I})(\mathbf{M}\mathbf{Z}_{\mathrm{c}}\mathbf{I} + \mathbf{V}_{\mathrm{i}})^{-1}$ representing the inverse of the gain of module capacitor voltage in the STATCOM, are almost linear at most frequencies except near the fundamental where it is affected by the module capacitor voltage control. Therefore, the elements in the transfer matrix $\mathbf{T}$ and the impedance coefficient matrix $\mathbf{Z}$ can be considered to have similar frequency characteristics.

To facilitate explanation, the transfer matrix $\mathbf{T}$ in (14) is divided into three parts and, respectively, denoted as

$$\mathbf{T}_1 = (\mathbf{U} - \mathbf{E}\mathbf{Z}_{\mathrm{c}}\mathbf{I})(\mathbf{M}\mathbf{Z}_{\mathrm{c}}\mathbf{I} + \mathbf{V}_{\mathrm{i}})^{-1}(\mathbf{Z}_{\mathrm{l}} + \mathbf{M}\mathbf{Z}_{\mathrm{c}}\mathbf{M})$$

$$\mathbf{T}_2 = \mathbf{Q}$$

$$\mathbf{T}_3 = \mathbf{E}\mathbf{Z}_{\mathrm{c}}\mathbf{M}.$$

Then, based on the analysis of the impedance characteristics described in [17], the elements in $\mathbf{T}_1$ are related to the arm inductor and submodule capacitor, which dominate the high-frequency characteristics of the (1, 3)-th and (3, 3)-th elements in $\mathbf{T}$; the elements in $\mathbf{T}_2$ are related to the phase current control, which dominate the characteristics of (3, 3)-th element in $\mathbf{T}$ below current control bandwidth frequency (except for those close to the fundamental); the elements in $\mathbf{T}_3$ are related to the module capacitor voltage control, which dominate the characteristics of the (1, 3)-th and (3, 3)-th elements in $\mathbf{T}$ close to the fundamental frequency, due to the typically low bandwidth of the associated control. In addition, since the gain of the dq-frame phase current control in the (1, 3)-th element of $\mathbf{T}_2$ is zero, the low- and medium-frequency characteristics of the (1, 3)-th element in matrix $\mathbf{T}$ are significantly affected by the (1, 3)-th element in matrix $\mathbf{T}_1$. The magnitude responses of the (1, 3)-th and (3, 3)-th elements in the transfer matrix $\mathbf{T}$, $\mathbf{T}_1$, $\mathbf{T}_2$, and $\mathbf{T}_3$ presented in Fig. 9 confirm the above analysis about the effects of each above part on the frequency characteristics of the elements in $\mathbf{T}$.

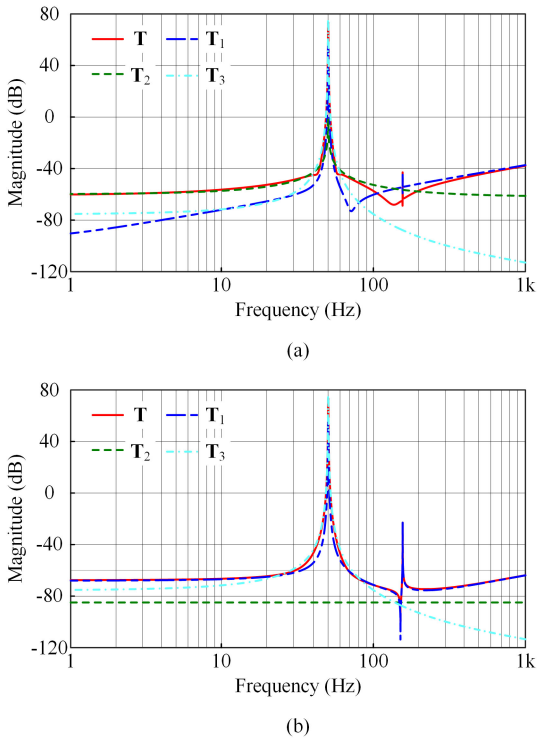

Fig. 9. Magnitude responses of (a) the (3, 3)-th element and (b) the (1, 3)-th element in the transfer matrix $\mathbf{T}$, $\mathbf{T}_1$, $\mathbf{T}_2$, and $\mathbf{T}_3$.

Therefore, in transfer matrix $\mathbf{T}_1$, $\mathbf{E}\mathbf{Z}_{\mathrm{c}}\mathbf{I}$ that only affects the frequency characteristics of elements in $\mathbf{T}_1$ near the fundamental frequency, and $\mathbf{M}\mathbf{Z}_{\mathrm{c}}\mathbf{I}$ that has few effects on the frequency characteristics of elements in $\mathbf{T}_1$ compared to $\mathbf{V}_{\mathrm{i}}$ can be ignored, and the transfer matrix $\mathbf{T}_1$ can be simplified as

$$\mathbf{T}_1 \approx \mathbf{V}_{\mathrm{i}}^{-1}(\mathbf{Z}_{\mathrm{l}} + \mathbf{M}\mathbf{Z}_{\mathrm{c}}\mathbf{M}). \tag{15}$$

In the expressions of elements in (15), the terms for $s + j\omega_1$ and $s - j\omega_1$ have a negligible effect on the high-frequency characteristics of both the (1, 3)-th and (3, 3)-th elements in $\mathbf{T}_1$, but the latter has a significant impact on the low- and medium-frequency characteristics of the (1, 3)-th element in matrix $\mathbf{T}_1$, and are thereby considered in the simplified expressions. Furthermore, since the high-frequency characteristics of the coupling term do not affect the system stability, the function terms for s in the (1, 3)-th element of (15) also can be removed. Finally, considering the relationship of the phase angle of each variable that σ_1

$\approx \beta_2/2 \approx \varphi_1$, the simplified (1, 3)-th and (3, 3)-th elements of $\mathbf{T}_1$ are denoted as

$$T_{s1(1,3)}(s) = e^{-j2\varphi_1}\frac{V_{i0}}{V_{i0}^2 - 2V_{i2}^2}\frac{M_1^2(1 - V_{i2}/V_{i0})}{(s - j\omega_1)C} \tag{16}$$

$$T_{s1(3,3)}(s) = \frac{V_{i0}}{V_{i0}^2 - 2V_{i2}^2}(sL + \frac{M_1^2(1 - V_{i2}/V_{i0})}{(s - j\omega_1)C}). \tag{17}$$

For the elements in $\mathbf{T}_2$, since they do not require to be simplified, its (1, 3)-th and (3, 3)-th elements can be directly given as

$$T_{s2(1,3)}(s) = e^{-j2\varphi_1}\frac{K_i}{2} \tag{18}$$

$$T_{s2(3,3)}(s) = H_i(s - j\omega_1) - jK_d + \frac{K_i}{2}. \tag{19}$$

With respect to $\mathbf{T}_3$, as the phase voltage balancing control is usually much slower than the average voltage control [26], the effect of the phase voltage balancing control on the frequency responses of elements in $\mathbf{T}_3$ can be ignored. Similarly, considering the relationship of the phase angle that $\sigma_1 \approx \varphi_1$, the simplified (1, 3)-th and (3, 3)-th elements of $\mathbf{T}_3$ are expressed as

$$T_{s3(1,3)}(s) = e^{-j2\varphi_1}\frac{M_1 H_i(s - j\omega_1)H_v(s - j\omega_1)}{2(s - j\omega_1)NC} \tag{20}$$

$$T_{s3(3,3)}(s) = \frac{M_1 H_i(s - j\omega_1)H_v(s - j\omega_1)}{2(s - j\omega_1)NC}. \tag{21}$$

Therefore, the simplified transfer matrix $\mathbf{T}$ is defined as $\mathbf{T}_s$, which is a 5 × 5 zero matrix except for the (1, 3)-th and (3, 3)-th elements, expressed as the sum of (16), (18), and (20), and the sum of (17), (19), and (21), respectively. A comparison of the frequency responses of the (1, 3)-th and (3, 3)-th elements in the transfer matrix $\mathbf{T}$ and $\mathbf{T}_s$ is presented in Fig. 10, which shows that the responses of the (1, 3)-th and (3, 3)-th elements of both are nearly identical over the most frequencies except for the high-frequency responses of the (1, 3)-th element, which confirms the rationality of simplification.

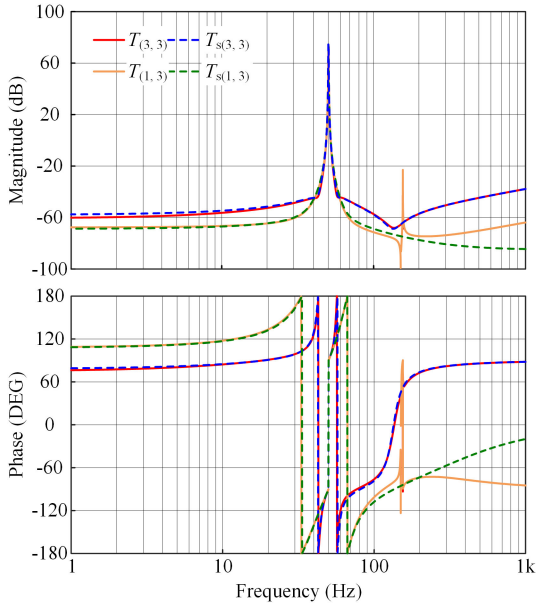

Fig. 10. Comparison of frequency responses of the (1, 3)-th and (3, 3)-th elements in the transfer matrix $\mathbf{T}$ and $\mathbf{T}_s$.

C. Implementation of Broadband Impedance Shaping Control

Using the simplified transfer matrix $\mathbf{T}_s$ to replace $\mathbf{T}$ in (14), the (1, 3)-th, and (3, 3)-th elements of $\mathbf{F}$ can be obtained as

$$F_{(1,3)}(s) = Y_{pi}(s)(T_{s1(1,3)}(s) + T_{s2(1,3)}(s) + T_{s3(1,3)}(s)) \tag{22}$$

$$F_{(3,3)}(s) = Y_{pi}(s)(T_{s1(3,3)}(s) + T_{s2(3,3)}(s) + T_{s3(3,3)}(s)). \tag{23}$$

Based on Fig. 8(c) as well as (22) and (23), the broadband impedance shaping control scheme for the single-star MMC-based STATCOM is implemented in Fig. 11 (without the transfer functions in the dashed block), where the red, blue, magenta and green parts in the control diagram are introduced by the expressions of $Y_{pi}(s)$, $T_{s1}(s)$, $T_{s2}(s)$, and $T_{s3}(s)$ in (22) and (23), respectively, and the transfer functions $G_{f1}(s)$, $G_{f2}(s)$, and $G_{f3}(s)$, respectively, are expressed as

$$G_{f1}(s) = \frac{sV_{i0}L}{V_{i0}^2 - 2V_{i2}^2}$$

$$G_{f2}(s) = \frac{2M_1^2(V_{i0} - V_{i2})}{(V_{i0}^2 - 2V_{i2}^2)C}\frac{1}{s}$$

$$G_{f3}(s) = \frac{M_1}{NC}\frac{1}{s}.$$

It is noted that the broadband impedance shaping control scheme presented in Fig. 11 also has an effect on the responses at the fundamental frequency, which may cause anomalies in the basic function of the STATCOM. To avoid this problem, a notch filter is added to eliminate the fundamental component in the broadband impedance shaping control scheme, expressed as

$$G_N(s) = \frac{s^2 + {\omega_1}^2}{s^2 + \zeta_1\omega_1 s + {\omega_1}^2} \tag{24}$$

where ζ_1 is the damping ratio.

In addition, the feedforward gain of the broadband impedance shaping control scheme must meet the Routh criterion, or the STATCOM with this control will lose its stability. Based on Fig. 11, the gains from u_d (u_q) to m_d (m_q) can be expressed as

$$\frac{m_{d1}}{u_d} = -G_{f12}(s) = -\frac{2M_1^2(V_{i0} - V_{i2})}{(V_{i0}^2 - 2V_{i2}^2)C}\frac{1}{s}$$

$$\frac{m_{d2}}{u_d} = \frac{m_q}{u_q} = -H_i(s) = -\frac{sK_{pi} + K_{ii}}{s}$$

$$\frac{m_{d3}}{u_d} = -G_{f3}(s)H_i(s)H_v(s)$$

$$= -\frac{M_1}{NC}\frac{(sK_{pi} + K_{ii})(sK_{pv} + K_{iv})}{s^3}.$$

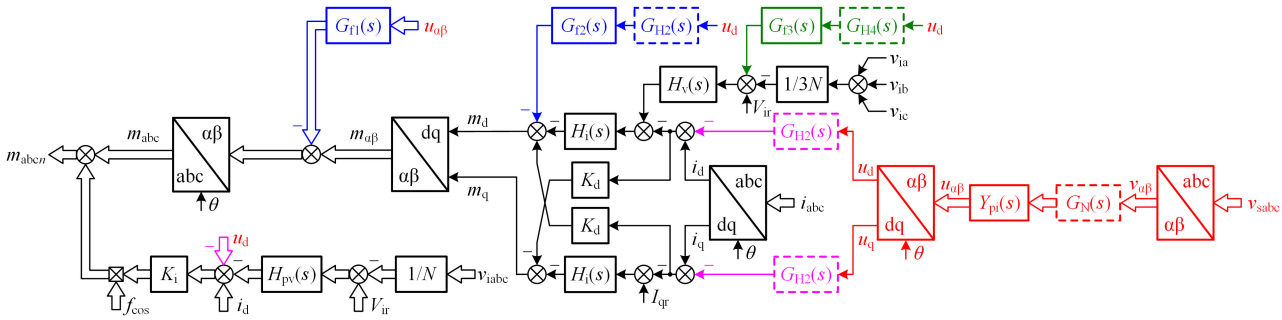

Fig. 11. Proposed broadband impedance shaping control scheme for the STATCOM in single-star MMC.

Obviously, the above gain functions do not meet the Routh criterion. Therefore, it is required to add a function with all the coefficients in the denominator polynomial being present and positive in the feedforward path, to eliminate the poles at $s = 0$ in the above gain functions, ensuring the stability of the STATCOM with the broadband impedance shaping control. Considering that such an additional function should be avoided as much as possible to affect the frequency responses of the feedforward gains at frequencies other than the fundamental frequency (the dc in the dq frame), the high-pass filter is the desired implementation of this function. Hence, according to the order of poles in the feedforward gains, a second-order high-pass filter and a fourth-order high-pass filters are introduced in the broadband impedance shaping control scheme and expressed as

$$G_{\mathrm{H2}}(s) = \frac{s^2}{s^2 + 2\zeta_2\omega_{\mathrm{n}}s + {\omega_{\mathrm{n}}}^2} \tag{25}$$

$$G_{\mathrm{H4}}(s) = G_{\mathrm{H2}}(s)G_{\mathrm{H2}}(s) = \frac{s^4}{\left(s^2 + 2\zeta_2\omega_{\mathrm{n}}s + {\omega_{\mathrm{n}}}^2\right)^2} \tag{26}$$

where ζ_2 is the damping ratio and ω_{n} is the undamped natural angular frequency.

In summary, the completed control diagram of the proposed broadband impedance shaping control scheme can be obtained by considering these filters in the dashed block in Fig. 11. Accordingly, based on Fig. 8(c), the admittance coefficient matrix of the STATCOM with proposed broadband impedance shaping control scheme is developed to be

$$\mathbf{Y}_{\mathrm{ST3}} = [(\mathbf{U} + \mathbf{Y}_{\mathrm{l}}\mathbf{M}\mathbf{Z}_{\mathrm{c}}\mathbf{M}) + \mathbf{Y}_{\mathrm{l}}(\mathbf{M}\mathbf{Z}_{\mathrm{c}}\mathbf{I} + \mathbf{V}_{\mathrm{i}})(\mathbf{U} - \mathbf{E}\mathbf{Z}_{\mathrm{c}}\mathbf{I})^{-1}\cdot (\mathbf{Q}+\mathbf{E}\mathbf{Z}_{\mathrm{c}}\mathbf{M})]^{-1}\mathbf{Y}_{\mathrm{l}}[\mathbf{U}-(\mathbf{M}\mathbf{Z}_{\mathrm{c}}\mathbf{I} + \mathbf{V}_{\mathrm{i}})(\mathbf{U}-\mathbf{E}\mathbf{Z}_{\mathrm{c}}\mathbf{I})^{-1}(\mathbf{P}-\mathbf{F}_{\mathrm{s}})] \tag{27}$$

where $\mathbf{F}_{\mathrm{s}}$ representing the control gain matrix related to the proposed broadband impedance shaping control scheme, is a 5×5 zero matrix except for the (1, 3)-th and (3, 3)-th elements, denoted, respectively, as

$$e^{-j2\varphi_1}Y_{\mathrm{pi}}(s)G_{\mathrm{N}}(s)\left[\frac{V_{\mathrm{i0}}M_1^2(1 - V_{\mathrm{i2}}/V_{\mathrm{i0}})G_{\mathrm{H2}}(s - j\omega_1)}{(s - j\omega_1)(V_{\mathrm{i0}}^2 - 2V_{\mathrm{i2}}^2)C} + \frac{K_{\mathrm{i}}}{2} + \frac{M_1H_{\mathrm{i}}(s - j\omega_1)H_{\mathrm{v}}(s - j\omega_1)G_{\mathrm{H4}}(s - j\omega_1)}{2(s - j\omega_1)NC}\right],$$

$$Y_{\mathrm{pi}}(s)G_{\mathrm{N}}(s)\left[(H_{\mathrm{i}}(s - j\omega_1) - jK_{\mathrm{d}})G_{\mathrm{H2}}(s - j\omega_1) + \frac{sV_{\mathrm{i0}}L}{V_{\mathrm{i0}}^2 - 2V_{\mathrm{i2}}^2} + \frac{K_{\mathrm{i}}}{2} + \frac{V_{\mathrm{i0}}M_1^2(1 - V_{\mathrm{i2}}/V_{\mathrm{i0}})G_{\mathrm{H2}}(s - j\omega_1)}{(s - j\omega_1)(V_{\mathrm{i0}}^2 - 2V_{\mathrm{i2}}^2)C} + \frac{M_1H_{\mathrm{i}}(s - j\omega_1)H_{\mathrm{v}}(s - j\omega_1)G_{\mathrm{H4}}(s - j\omega_1)}{2(s - j\omega_1)NC}\right].$$

V. Design of Impedance Shaping Controller

According to Section IV, the parallel impedance produced by the proposed impedance shaping control scheme can be approximated as $Y_{\mathrm{pi}}(s)$ except near the fundamental frequency, and its characteristics are independent of the parameters of the regulator for the inherent control loops in the STATCOM, e.g., the phase current control loop and the average voltage control loop. Therefore, the design of the broadband impedance shaping controller is essentially the design of the desired parallel impedance, namely $Y_{\mathrm{pi}}(s)$. The transfer function of $Y_{\mathrm{pi}}(s)$ can be designed as any polynomial, as long as it causes the feedforward gain of the broadband impedance shaping control to satisfy the Routh criterion. However, as aforementioned, in order to obtain sufficient damping to mitigate the system resonances, both the amplitude and phase of $Y_{\mathrm{pi}}(s)$ should be designed, which poses difficulties in its parameter design, especially for those with complex higher-order transfer functions. Therefore, a simple passivity-based design method for the parallel impedance is developed in this section. Taking the cases in Section III as an example, to provide sufficient damping at the sub and super-synchronous frequency for the entire wind farm, the parallel impedance is defined as a series RL circuit:

$$Y_{\mathrm{pi}}(s) = \frac{1}{sL_{\mathrm{v}} + R_{\mathrm{v}}} \tag{28}$$

Then, an equivalent RLC circuit model is introduced to passively simplify the wind farm impedance. Specifically, $Y_{\mathrm{ewf}}(s)$ can be approximated as a second-order series RLC circuit in the frequency range $\{\omega \,|\, 0 \le |\omega - \omega_{\mathrm{i}}| < \delta\}$ (δ is a very small positive constant), denoted as

$$Y_{\mathrm{ewf}}(s) = \frac{sC_{\mathrm{e}}}{s^2L_{\mathrm{e}}C_{\mathrm{e}} + sC_{\mathrm{e}}R_{\mathrm{e}} + 1} \tag{29}$$

where R_{e} is obtained by $R_{\mathrm{e}} = \mathrm{Re}[Z_{\mathrm{ewf}}(j\omega_{\mathrm{i}})]$, and L_{e} and C_{e} are solved by the following optimal approximation problem using

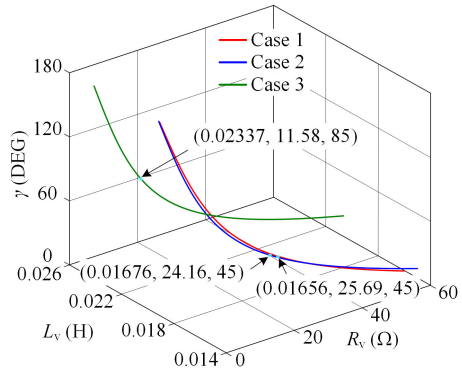

Fig. 12. Relationship between the stability margin and the parallel impedance.

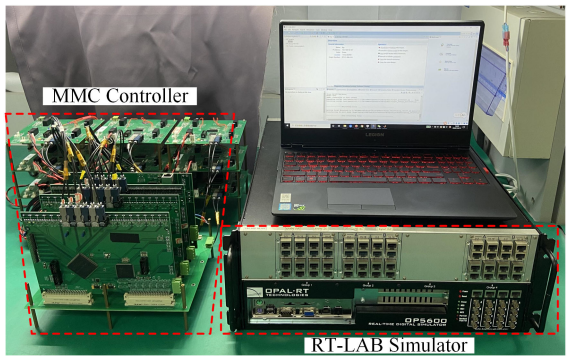

Fig. 13. RT-LAB simulator-based HIL experimental platform.

Matlab's curve-fitting function "lsqcurvefit" [32]:

$$\min \left\| \omega L_{\mathrm{e}} - \frac{1}{\omega C_{\mathrm{e}}} - \mathrm{Im}[Z_{\mathrm{ewf}}(j\omega_{\mathrm{i}})] \right\|^2$$
$$\text{s.t.}\ \omega_{\mathrm{i}} L_{\mathrm{e}} - \frac{1}{\omega_{\mathrm{i}} C_{\mathrm{e}}} = \mathrm{Im}[Z_{\mathrm{ewf}}(j\omega_{\mathrm{i}})];\ L_{\mathrm{e}}, C_{\mathrm{e}} > 0. \tag{30}$$

Since $Y_{\mathrm{pi}}(s)$ is equivalent to a direct parallel connection to the PCC of the wind farm, the wind farm admittance with the proposed STATCOM broadband impedance shaping control scheme can be approximated as a parallel admittance $Y_{\mathrm{wf\_shp}}(\mathrm{s})$ of $Y_{\mathrm{ewf}}(s)$ and $Y_{\mathrm{pi}}(s)$ by ignoring the additional coupling responses caused by the parallel impedance in this design method. Based on (28) and (29), $Y_{\mathrm{wf\_shp}}(\mathrm{s})$ is expressed as

$$Y_{\mathrm{wf\_shp}}(s) = \frac{s^2 C_{\mathrm{e}}(L_{\mathrm{e}} + L_{\mathrm{v}}) + sC_{\mathrm{e}}(R_{\mathrm{e}} + R_{\mathrm{v}}) + 1}{s^3 L_{\mathrm{e}} L_{\mathrm{v}} C_{\mathrm{e}} + s^2 C_{\mathrm{e}}(L_{\mathrm{e}} R_{\mathrm{v}} + L_{\mathrm{v}} R_{\mathrm{e}}) + s(L_{\mathrm{v}} + C_{\mathrm{e}} R_{\mathrm{e}} R_{\mathrm{v}}) + R_{\mathrm{v}}} \tag{31}$$

According to the definition of the equivalent RLC circuit for the wind farm in (29), $Y_{\mathrm{wf\_shp}}(\mathrm{s})$ only holds when the frequency is much closer to ω_{i}. Therefore, in order to be able to use (31) to evaluate the stability margin of the wind farm system with the proposed STATCOM broadband impedance shaping control scheme, the intersection frequency of the wind farm impedance with or without the additional virtual impedance and the grid impedance is required to remain constant, that is,

$$\|Y_{\mathrm{wf\_shp}}(j\omega_{\mathrm{i}})\| = \|Y_{\mathrm{ewf}}(j\omega_{\mathrm{i}})\| \tag{32}$$

In this case, by solving (32), the relationship between L_{v} and R_{v} is obtained as

$$L_{\mathrm{v}} = \frac{(1 - \omega_{\mathrm{i}}^2 L_{\mathrm{e}} C_{\mathrm{e}})^2 + (\omega_{\mathrm{i}} C_{\mathrm{e}} R_{\mathrm{e}})^2 + 2\omega_{\mathrm{i}}^2 C_{\mathrm{e}}^2 R_{\mathrm{e}} R_{\mathrm{v}}}{2\omega_{\mathrm{i}}^2 C_{\mathrm{e}}(1 - \omega_{\mathrm{i}}^2 L_{\mathrm{e}} C_{\mathrm{e}})} \tag{33}$$

Finally, using this constraint in (33), a set of parameters of the parallel impedance can be exclusively determined by the desired stability margin γ which is obtained by replacing $Z_{\mathrm{ewf}}(j\omega_{\mathrm{i}})$ in (11) with the inverse of $Y_{\mathrm{wf\_shp}}(j\omega_{\mathrm{i}})$ in (31). Fig. 12 illustrates the relationship between the stability margin and the parallel impedance for the cases in Section III. In general, the stability margin of between 30° and 60° is appropriate. Considering the possible stability margin attenuation caused by the frequency coupling effect, the stability margin in the design is set to 45°, 45°, and 85° for these three cases, respectively, and the corresponding parameters of parallel impedance can be obtained from Fig. 12 as $R_{\mathrm{v}} = 25.69\ \Omega$ and $L_{\mathrm{v}} = 0.01656$ H for Case 1, $R_{\mathrm{v}} = 24.16\ \Omega$ and $L_{\mathrm{v}} = 0.01676$ H for Case 2, and $R_{\mathrm{v}} = 11.58\ \Omega$ and $L_{\mathrm{v}} = 0.02337$ H for Case 3.

Additionally, the parameters of the filters $G_{\mathrm{N}}(s)$ and $G_{\mathrm{H2}}(s)$ used in the proposed broadband impedance shaping control scheme can be designed by -3dB bandwidth design method. When shaping the STATCOM impedance at sub and super-synchronous frequencies, the bandwidth of the filter should be much smaller than the bandwidth of the average voltage control loop, to ensure that the parallel impedance implemented by the control remains valid near the fundamental frequency. Of course, too small a filter bandwidth is equally undesirable, which will affect the ability of the STATCOM to deal with sudden changes in the system operating conditions. In this article, the bandwidth of $G_{\mathrm{N}}(s)$ and $G_{\mathrm{H2}}(s)$ are both designed as 1 Hz and the damping ratio of $G_{\mathrm{H2}}(s)$ is set as $\zeta_2 = 0.707$, resulting in that $\zeta_1 = 0.04$ and $\omega_{\mathrm{n}} = 6.28$ rad/s.

VI. Verification By HIL Experiments

A HIL experimental platform is built in the lab to verify the effectiveness of the proposed MMC-based STATCOM broadband impedance shaping control scheme for the improvement of system stability, as shown in Fig. 13. The configuration of wind farm system is presented in Fig. 3, where the WTGs, the grid, and the power stage of the MMC-based STATCOM are emulated in a RT-LAB OP5600 simulator and the STATCOM controls are implemented by a developed MMC controller, which consist of the master controller, slave controllers for each phase, high-speed LVDS board-to-board data transmission, and optical fiber communications. The parameters of the aggregated type-IV WTG and the wind farm system are presented in Tables II and III, respectively. The parameters of the STATCOM are mostly the same as shown in Table I, however, the number of modules per arm of the STATCOM in this HIL experiment have to be reduced from 36, in Table I, to 3 due to the limitation of the numbers of digital-in (DI) channels in this RT-LAB simulator. Accordingly, the submodule capacitance and the coefficients in

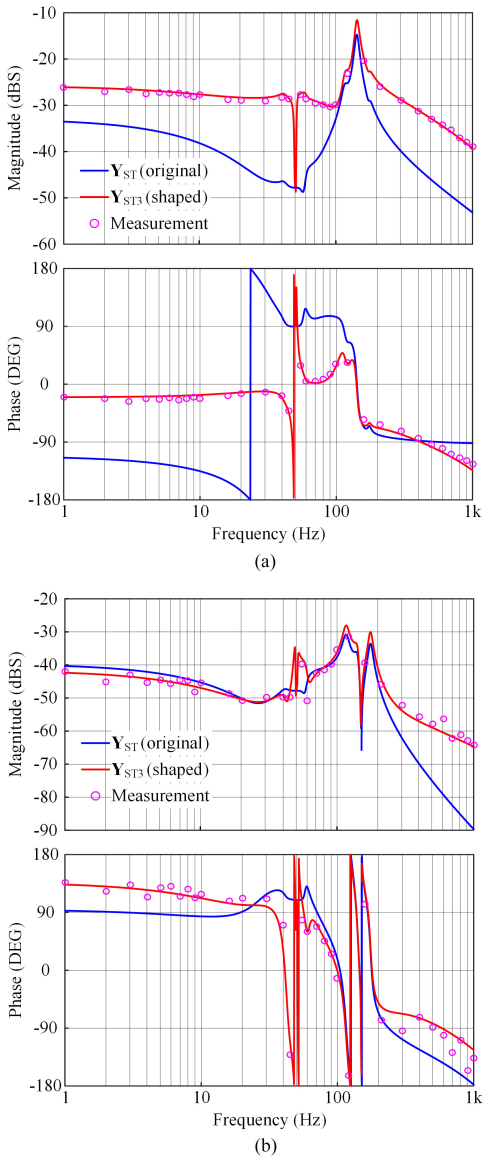

Fig. 14. Frequency responses of (a) $Y_{\mathrm{p}}(s)$ and (b) $Y_{\mathrm{c}}(s)$ in the admittance matrix of $\mathbf{Y}_{\mathrm{ST}}$ (original) and $\mathbf{Y}_{\mathrm{ST3}}$ (shaped).

$H_{\mathrm{v}}(s)$ and $H_{\mathrm{pv}}(s)$ are required to be divided by 12 and the cell capacitor voltage needs to be multiplied by 12, which ensure that the dynamics of the STATCOM below half the equivalent switching frequency is not affected by the decreasing number of modules.

Taking the parameters of the impedance shaping controller designed for Case 1 as an example, Fig. 14 depicts the frequency responses of the transfer functions in the admittance matrix (9) and (29), representing the STATCOM without and with the proposed broadband impedance shaping control scheme, respectively. The correctness of developed models is verified by comparing the predicted frequency responses for the STATCOM with proposed broadband impedance shaping control scheme with the frequency-scanning responses obtained by the measurement based on this HIL experimental platform. In addition, as can be seen, comparing with the responses for the STATCOM

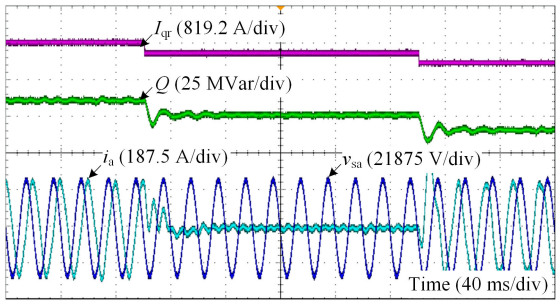

Fig. 15. Dynamic and steady-state performance of the STATCOM with the broadband impedance shaping control scheme.

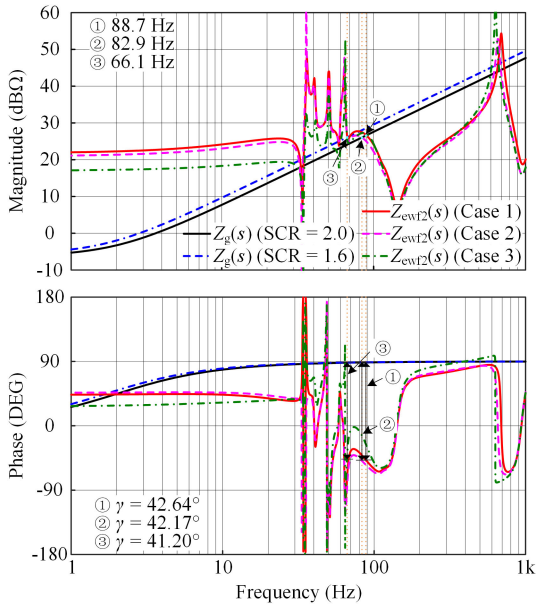

Fig. 16. Frequency responses of $Z_{\mathrm{g}}(s)$ and $Z_{\mathrm{ewf2}}(s)$ for studied cases.

without the impedance shaping control, the proposed control mainly affects $Y_{\mathrm{p}}(s)$, which enables a complete simulation of the parallel impedance (series RL circuit) by reshaping both magnitude and phase responses of the impedance over a wide frequency range. The phase responses of the reshaped $Y_{\mathrm{p}}(s)$ are close to 0° at the low- and medium-frequencies, that is, the MMC-based STATCOM impedance mainly exhibits resistive characteristics at sub and super-synchronous frequencies, which ensures that it can provide positive damping to enhance the stability-robustness of the wind farm system without other potential negative impacts. On the other hand, the magnitude responses of the reshaped $Y_{\mathrm{p}}(s)$, which roughly double several times at sub and super-synchronous frequencies, allows the MMC-based STATCOM, whose rated power represents only 20% of the power of the wind farm, to achieve the impedance control of the entire wind farm for effective resonance suppression.

A. Dynamic and Steady-State Performance

Again using the parameters of the impedance shaping controller designed for Case 1 as an example, the dynamic and

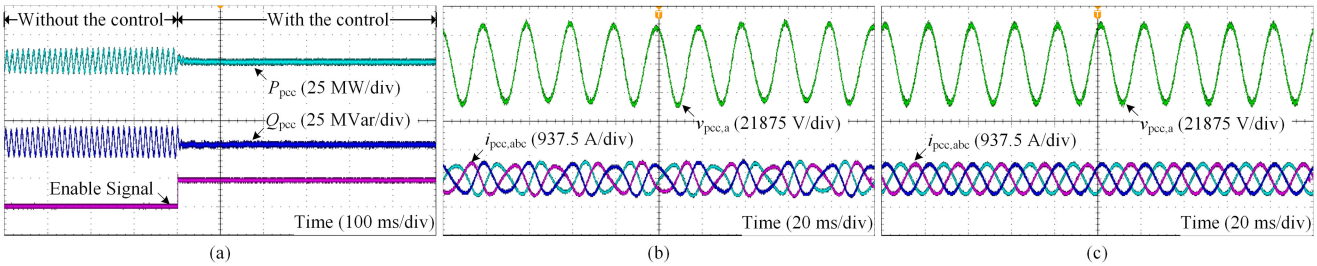

Fig. 17. HIL experimental results of the wind farm for the STATCOM without and with the broadband impedance shaping control scheme in Case 1: (a) the output powers; (b) PCC voltage and injected currents without the proposed control; (c) PCC voltage and injected currents with the proposed control.

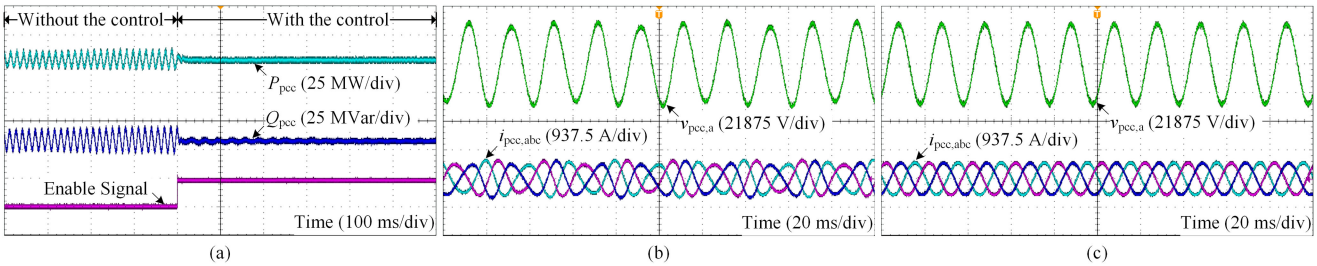

Fig. 18. HIL experimental results of the wind farm for the STATCOM without and with the broadband impedance shaping control scheme in Case 2: (a) the output powers; (b) PCC voltage and injected currents without the proposed control; (c) PCC voltage and injected currents with the proposed control.

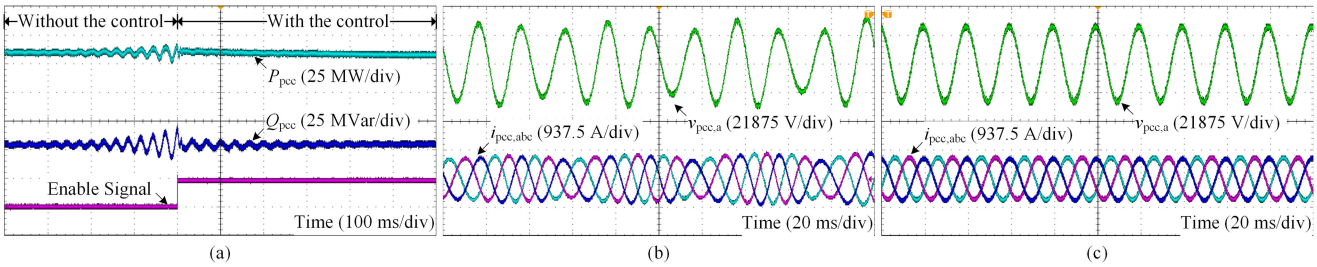

Fig. 19. HIL experimental results of the wind farm for the STATCOM without and with the broadband impedance shaping control scheme in Case 3: (a) the output powers; (b) PCC voltage and injected currents without the proposed control; (c) PCC voltage and injected currents with the proposed control.

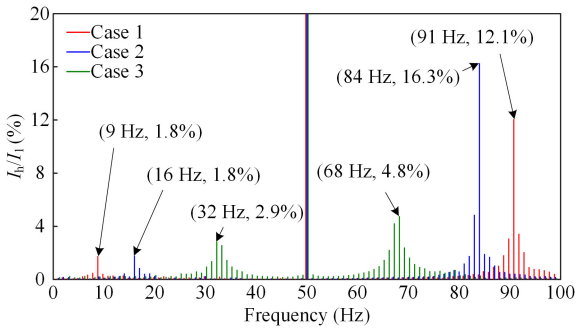

Fig. 20. FFT results of the injected current of the wind farm for the STATCOM without the proposed control in studied cases.

steady-state performance of the STATCOM with the proposed broadband impedance shaping control scheme is examined based on this HIL experimental platform. In the experiments, the reactive current reference I_{qr} is first stepped from absorbing inductive reactive rated power to no-load, and then from no-load to absorbing capacitive reactive rated power, as shown in Fig. 15. It should be noted that the amplitude of signals captured from the analog-out (AO) channels of the RT-LAB simulator is scaled down, therefore, to facilitate observation, the amplitude labeled in the experimental waveforms is uniformly used with their original nominal value. It can be seen from Fig. 15 that the reactive power Q tracks the step reference well, and the corresponding transient current has a short settling time and small overshoots. Moreover, the total harmonic distortion (THD) of the steady-state current in full-load for absorbing inductive and capacitive reactive power is both less than 5%, at 3.1% and 3.6%, respectively, which meet the requirements for the converter connected to the grid. These indicate that the dynamic and steady-state performance as well as the basic function of the STATCOM with this additional broadband impedance shaping control scheme can be guaranteed.

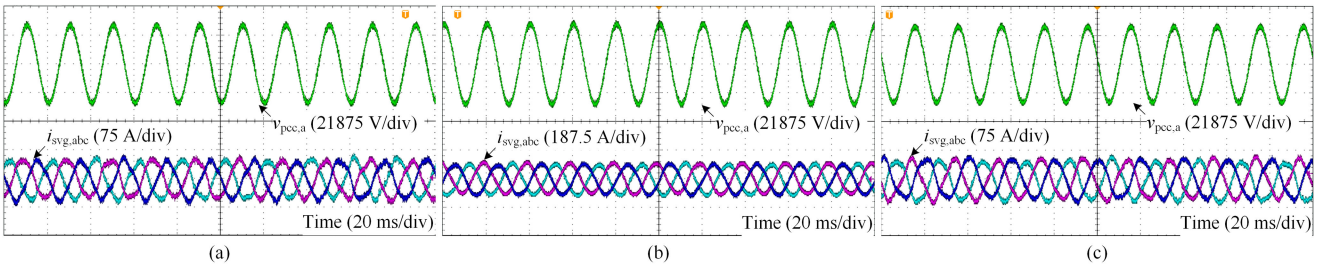

Fig. 21. HIL experimental results of the PCC voltage and output currents of the STATCOM when the broadband impedance shaping control scheme is enabled in (a) Case 1, (b) Case 2, and (c) Case 3.

B. Improvement of System Stability

The studied wind farm presented in Section III is exemplified in this section to demonstrate the effect of the proposed STATCOM broadband impedance shaping control scheme on the system stability. With the broadband impedance shaping control in the STATCOM, there are no RHP zeros in the determinant of the frequency-domain nodal admittance matrix of the system for all three cases. Fig. 16 presents the frequency responses of the grid impedance and the equivalent impedance of the wind farm to further assess the stability margin, where $Z_{ewf2}(s)$ represents the equivalent impedance of the wind farm for the STATCOM with the broadband impedance shaping control scheme obtained by (10). It can be found that, compared to the situations of the wind farm without the STATCOM impedance shaping control in Fig. 6, the intersection of $Z_g(s)$ and $Z_{ewf2}(s)$ is slightly shifted and the corresponding stability margin of the wind farm is substantially increased, where it is increased from –1.98° to 42.64° in Case 1, from –1.49° to 42.17° in Case 2, and from approximately 0° to 41.20° in Case 3. This shows that the STATCOM with the broadband impedance shaping control scheme can effectively suppress the wind farm resonance caused by the negative damping under various operation conditions. Additionally, benefiting from the impedance shaping capability over a wide frequency of the proposed control, the damping of the equivalent impedance of the wind farm is greatly improved in the vicinity of the intersection frequency used in the design. This not only ensures the applicability of the proposed control when the intersection frequency varies slightly and the stability margin is lower than the design due to the consideration of the frequency coupling effects, but also enhances the robustness against the variations of the grid condition.

Figs. 17–19 present the HIL experimental results of the wind farm for the STATCOM without and with the proposed broadband impedance shaping control scheme in Cases 1, 2, and 3, respectively. Without the broadband impedance shaping control, the resonance occurs and gradually diverges in the output powers, PCC voltages, and injected currents in all three cases, as shown in (a) and (b) of Figs. 17–19. The THD of the injected currents in (b) of Figs. 17–19 are 13.7%, 17.6%, and 9.6%, and the corresponding fast Fourier transformation (FFT) results presented in Fig. 20 identify the dominant resonance frequencies are 9 and 91 Hz in Case 1, 16 and 84 Hz in Case 2, and 32 and 68 Hz in Case 3. In contrast, when the broadband impedance shaping control is enabled, the resonances in the output power, PCC voltages, and injected currents of the wind farm are completely and quickly suppressed, as illustrated in (a) and (c) of Figs. 17–19. The THD of the injected currents in (b) of Figs. 17–19 are reduced to 1.3%, 1.0%, and 0.8%, respectively. Obviously, the above HIL experimental results all agree with the impedance-based stability analysis in Figs. 6 and 16, which confirms the proposed STATCOM broadband impedance shaping control scheme.

In addition, Fig. 21 illustrates the HIL experimental results of the PCC voltage and output currents of the STATCOM when the broadband impedance shaping control scheme is enabled in three cases. The output currents of the STATCOM without resonance indicates that the effect of the proposed impedance shaping control is in using the frequency-domain impedance of the STATCOM to provide the damping for the system resonance mitigation, not in adding an active filtering function to absorb the resonant currents. Therefore, even if the STATCOM is already working near its physical limits, the basic reactive power compensation function of the STATCOM is not affected, and there is no need to increase the capacity of the STATCOM in order to achieve this proposed control.

VII. Conclusion

The STATCOM, which has been installed in the wind farm in certain regions, is an effective and economical option for shaping the output impedance to damp the sub and super-synchronous resonance of the wind farm and improve the system stability-robustness. Instead of regulating the controller parameters in the STATCOM, this article proposes a broadband impedance shaping control scheme for reshaping the STATCOM impedance characteristics over the sub and super-synchronous frequencies. Based on the sequence equivalent control block diagram of the MMC-based STATCOM that includes the impacts of the multiharmonic characteristics of MMC and frequency coupling effect, an active parallel impedance is derived and employed to shape its output impedance for improving the system damping over a wide frequency range, especially covering the sub and super-synchronous frequencies. On the other hand, benefiting from that this active impedance does not depend on the parameters design of the inherent control loops in the STATCOM, a passivity-based design method is developed to independently

design the active impedance to ensure that the proposed control can provide sufficient damping over the entire sub and synchronous frequency range. Therefore, with the proposed broadband impedance shaping control scheme, the STATCOM exhibits strong damping ability and the stability-robustness of the wind farm is improved accordingly. This not only protects the interests of wind farm owners, but also further enhances the value of STATCOM. Experimental results based on the HIL platform confirm the effectiveness of the proposed control under various operation conditions of the wind farm.

REFERENCES

[1] J. Adams, V. A. Pappu, and A. Dixit, "Ercot experience screening for subsynchronous control interaction in the vicinity of series capacitor banks," in *Proc. IEEE Power Eng. Soc. Gen. Meeting*, Jul. 2012, pp. 1–5.

[2] X. X. L.Wang, Q. Jiang, H. Liu, Y. Li, and H. Liu, "Investigation of SSR in practical DFIG-based wind farms connected to a series-compensated power system," *IEEE Trans. Power Syst.*, vol. 30, no. 5, pp. 2772–2779, Sept. 2015.

[3] H. Liu *et al.*, "Subsynchronous interaction between direct-drive PMSG based wind farms and weak AC networks," *IEEE Trans. Power Syst.*, vol. 32, no. 6, pp. 4708–4720, Nov. 2017.

[4] J. Sun *et al.*, "Renewable energy transmission by HVDC across the continent: System challenges and opportunities," *CSEE J. Power Energy Syst.*, vol. 3, no. 4, pp. 353–364, Dec. 2017.

[5] J. Sun, "Impedance-based stability criterion for grid-connected inverters," *IEEE Trans. Power Electron.*, vol. 26, no. 11, pp. 3075–3078, Nov. 2011.

[6] J. Lyu, X. Cai, and M. Molinas, "Frequency domain stability analysis of MMC-based HVdc for wind farm integration," *IEEE J. Emerg. Sel. Topics Power Electron.*, vol. 4, no. 1, pp. 141–151, Mar. 2016.

[7] H. Liu and J. Sun, "Voltage stability and control of offshore wind farms with AC collection and HVDC transmission," *IEEE J. Emerg. Sel. Topics Power Electron.*, vol. 2, no. 4, pp. 1181–1189, Dec. 2014.

[8] H. Liu, X. Xie, Y. Li, H. Liu, and Y. Hu, "Mitigation of SSR by embedding subsynchronous notch filters into DFIG converter controllers," *IET Gener. Transmiss. Dis.*, vol. 11, no. 11, pp. 2888–2896, Sep. 2017.

[9] H. Chen, P. Cheng, X. Wang, and F. Blaabjerg, "A passivity-based stability analysis of the active damping technique in the offshore wind farm applications," *IEEE Trans. Ind. Appl.*, vol. 54, no. 5, pp. 5074–5082, Sep./Oct. 2018.

[10] X. Wang, F. Blaabjerg, M. Liserre, Z. Chen, J. He, and Y. Li, "An active damper for stabilizing power-electronics-based AC systems," *IEEE Trans. Power Electron.*, vol. 29, no. 7, pp. 3318–3329, Jul. 2014.

[11] L. Jia, X. Ruan, W. Zhao, Z. Lin, and X. Wang, "An adaptive active damper for improving the stability of grid-connected inverters under weak grid," *IEEE Trans. Power Electron.*, vol. 33, no. 11, pp. 9561–9574, Nov. 2018.

[12] L. Wang and D. Truong, "Stability enhancement of DFIG-based offshore wind farm fed to a multi-machine system using a STATCOM," *IEEE Trans. Power Syst.*, vol. 28, no. 3, pp. 2882–2889, Aug. 2013.

[13] A. Moharana, R. K. Varma, and R. Seethapathy, "SSR alleviation by STATCOM in induction-generator-based wind farm connected to series compensated line," *IEEE Trans. Sustain. Energy*, vol. 5, no. 3, pp. 947–957, Jul. 2014.

[14] D. Shu, X. Xie, H. Rao, X. Gao, Q. Jiang, and Y. Huang, "Sub- and super-synchronous interactions between STATCOMs and weak ac/dc transmissions with series compensations," *IEEE Trans. Power Electron.*, vol. 33, no. 9, pp. 7424–7437, Sep. 2018.

[15] C. Li, R. Burgos, B. Wen, Y. Tang, and D. Boroyevich, "Analysis of STATCOM small-signal impedance in the synchronous d-q frame," *IEEE J. Emerg. Sel. Topics Power Electron.*, vol. 8, no. 2, pp. 1894–1910, Jun. 2020.

[16] G. Li, Y. Chen, A. Luo, and H. Wang, "An enhancing grid stiffness control strategy of STATCOM/BESS for damping sub-synchronous resonance in wind farm connected to weak grid," *IEEE Trans. Ind. Inform.*, vol. 16, no. 9, pp. 5835–5845, Sep. 2020.

[17] Y. Zhang, X. Chen, and J. Sun, "Sequence impedance modeling and analysis of MMC in single-star configuration," *IEEE Trans. Power Electron.*, vol. 35, no. 1, pp. 334–346, Jan. 2020.

[18] C. Li, R. Burgos, B. Wen, Y. Tang, and D. Boroyevich, "Stability analysis of power systems with multiple STATCOMs in close proximity," *IEEE Trans. Power Electron.*, vol. 35, no. 3, pp. 2268–2283, Mar. 2020.

[19] Y. Zhang, Y. Yang, X. Chen, and C. Gong, "Intelligent parameter design-based impedance optimization of STATCOM to mitigate resonance in wind farms," *IEEE J. Emerg. Sel. Topics Power Electron.*, doi: 10.1109/JESTPE.2020.3020434.

[20] A. Aapro, T. Messo, T. Roinila, and T. Suntio, "Effect of active damping on output impedance of three-phase grid-connected converter," *IEEE Trans. Ind. Electron.*, vol. 64, no. 9, pp. 7532–7541, Sep. 2017.

[21] J. He, Y. W. Li, D. Bosnjak, and B. Harris, "Investigation and active damping of multiple resonances in a parallel-inverter-based microgrid," *IEEE Trans. Power Electron.*, vol. 28, no. 1, pp. 234–246, Jan. 2013.

[22] D. Pan, X. Ruan, C. Bao, W. Li, and X. Wang, "Capacitor-current-feedback active damping with reduced computation delay for improving robustness of LCL-type grid-connected inverter," *IEEE Trans. Power Electron.*, vol. 29, no. 7, pp. 3414–3427, Jul. 2014.

[23] J. Xu, S. Xie, B. Zhang, and Q. Qian, "Robust grid current control with impedance-phase shaping for LCL-filtered inverters in weak and distorted grid," *IEEE Trans. Power Electron.*, vol. 33, no. 12, pp. 10240–10250, Dec. 2018.

[24] D. Yang, X. Ruan, and H. Wu, "Impedance shaping of the grid-connected inverter with LCL filter to improve its adaptability to the weak grid condition," *IEEE Trans. Power Electron.*, vol. 29, no. 11, pp. 5795–5805, Nov. 2014.

[25] X. Chen, Y. Zhang, S. Wang, J. Chen, and C. Gong, "Impedance-phased dynamic control method for grid-connected inverters in a weak grid," *IEEE Trans. Power Electron.*, vol. 32, no. 1, pp. 274–283, Jan. 2017.

[26] H. Akagi, S. Inoue, and T. Yoshii, "Control and performance of a transformerless cascade PWM STATCOM with star configuration," *IEEE Trans. Ind. Appl.*, vol. 43, no. 4, pp. 1041–1049, Jul./Aug. 2007.

[27] J. Sun and H. Liu, "Sequence impedance modeling of modular multilevel converters," *IEEE J. Emerg. Sel. Topics Power Electron.*, vol. 5, no. 4, pp. 1427–1443, Dec. 2017.

[28] H. Wang, I. Vieto, and J. Sun, "A method to aggregate turbine and network impedances for wind farm system resonance analysis," in *Proc. IEEE 19th Workshop Control Model. Power Electron.*, Jun. 2018, pp. 1–8.

[29] Y. Zhan, X. Xie, H. Liu, H. Liu, and Y. Li, "Frequency-domain modal analysis of the oscillatory stability of power systems with high-penetration renewables," *IEEE Trans. Sustain. Energy*, vol. 10, no. 3, pp. 1534–1543, Jul. 2019.

[30] C. Zhang, M. Molinas, A. Rygg, and X. Cai, "Impedance-based analysis of interconnected power electronics systems: Impedance network modeling and comparative studies of stability criteria," *IEEE J. Emerg. Sel. Topics Power Electron.*, vol. 8, no. 3, pp. 2520–2533, Sep. 2020.

[31] X. Wang, Y. W. Li, F. Blaabjerg, and P. C. Loh, "Virtual-impedance-based control for voltage-source and current-source converters," *IEEE Trans. Power Electron.*, vol. 30, no. 12, pp. 7019–7037, Dec. 2015.

[32] H. Liu, X. Xie, C. Zhang, Y. Li, H. Liu, and Y. Hu, "Quantitative SSR analysis of series-compensated DFIG-based wind farms using aggregated RLC circuit model," *IEEE Trans. Power Syst.*, vol. 32, no. 1, pp. 474–483, Jan. 2017.

Yang Zhang (Member, IEEE) received the B.S. and M.S. degrees in electrical engineering in 2012 and 2015, respectively, from the Nanjing University of Aeronautics and Astronautics, Nanjing, China, where he is currently working toward the Ph.D. degree in electrical engineering.

His main research interests include the renewable generation system modeling, stability analysis and control.

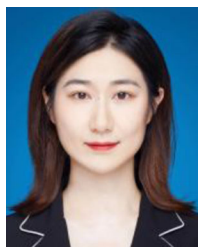

Yuqing Wang was born in Xi'an, Shaanxi, China. She received the B. S. degree in electrical engineering and automation in 2018 from Nanjing University of Aeronautics and Astronautics, Nanjing, China, where she is currently working toward the M.S. degree in electrical engineering.

Her main research interests include modeling and system stability of renewable power system.

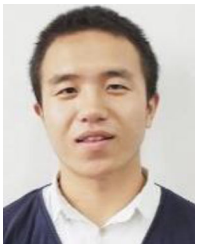

Donghui Zhang received the B.S. degree and M.S. degree in electrical engineering from Shanxi Datong University, Datong, China, Hunan University of Technology, Zhuzhou, China, in 2017 and 2020, respectively. He is currently working toward the Ph.D. degree with Nanjing University of Aeronautics and Astronautics, Nanjing, China.

His research interests include control and stability analysis of power systems with large-scale renewable energy generations and high voltage dc (HVdc) transmission, in particular on modeling and stability analysis of power electronic devices.

Xin Chen (Member, IEEE) received the B.S. and Ph.D. degrees in electrical engineering from Nanjing University of Aeronautics and Astronautics, Nanjing, China, in 1996 and 2001, respectively.

He is a Professor of Department of Electrical Engineering, Nanjing University of Aeronautics and Astronautics. He was a Chief Engineer (2001–2003) in Power Division of ZTE Corporation, and a Visiting Scholar (2010–2011) at the Rensselaer Polytechnic Institute, Troy, USA. His current research interests include modeling, control and stability of distributed generation and microgrid systems.

Chunying Gong (Member, IEEE) was born in Zhejiang, China, in 1965. She received the B.S., M.S., and Ph.D. degrees in electrical engineering from Nanjing University of Aeronautics and Astronautics (NUAA), Nanjing, China, in 1984, 1990, and 1993, respectively.

From 1984 to 1987, she was an Electrical Assistant Engineer with Chengdu Aircraft Design and Research Institute. In 1993, she joined as a Lecturer with the College of Automation Engineering, NUAA, where she became an Associate Professor in 1996 and a Professor in 2004. In 2009, she was a Visiting Scholar in the Department of Electrical, Computer, and Systems Engineering, Rensselaer Polytechnic Institute, New York, NY, USA. She is the author or co-author of more than 100 technical papers published in journals and conference proceedings. Her research focuses on static inverters, power electronic systems stability and power quality, renewable energy, and distributed generation.